BNL-108271-2015-JA

An Array of Virtual Frisch-grid CdZnTe Detectors and a Front-End ASIC for Large-Area Position-Sensitive Gamma-Ray Cameras

A. Bolotnikov

Submitted to the Review of Scientific Instruments

August 2015

Nonproliferation and National Security Department

Brookhaven National Laboratory
P.O. Box 5000
Upton, New York 11973
Bnl.gov

U.S. Department of Energy
Office of Nonproliferation and Verification Research and Development (NA-22)

Notice: This manuscript has been authored by employees of Brookhaven Science Associates, LLC under Contract No. DE-AC02-98CH10886 with the U.S. Department of Energy. The publisher by accepting the manuscript for publication acknowledges that the United States Government retains a non-exclusive, paid-up, irrevocable, world-wide license to publish or reproduce the published form of this manuscript, or allow others to do so, for United States Government purposes.

DISCLAIMER

This report was prepared as an account of work sponsored by an agency of the United States Government. Neither the United States Government nor any agency thereof, nor any of their employees, nor any of their contractors, subcontractors, or their employees, makes any warranty, express or implied, or assumes any legal liability or responsibility for the accuracy, completeness, or any third party's use or the results of such use of any information, apparatus, product, or process disclosed, or represents that its use would not infringe privately owned rights. Reference herein to any specific commercial product, process, or service by trade name, trademark, manufacturer, or otherwise, does not necessarily constitute or imply its endorsement, recommendation, or favoring by the United States Government or any agency thereof or its contractors or subcontractors. The views and opinions of authors expressed herein do not necessarily state or reflect those of the United States Government or any agency thereof.

An array of virtual Frisch-grid CdZnTe detectors and a front-end ASIC for large-area position-sensitive gamma-ray cameras

A. E. Bolotnikov[1a)], K. Ackley[1], G. S. Camarda[1], C. Cherches[1], Y. Cui[1], G. De Geronimo[1], J. Fried[1], D. Hodges[2], A. Hossain[1], W. Lee[3], G. Mahler[1], M. Maritato[1], M. Petryk[4], U. Roy[1], C. Salwen[1], E. Vernon[1], G. Yang[1], and R. B. James[1]

[1]*Brookhaven National Laboratory, Upton, NY 11793, USA*

[2]*University of Texas at El Paso, El Paso, TX 79968, USA*

[3]*Korea University, Seoul, 136-855, South Korea*

[4]*SUNY Binghamton, Vestal, NY 13902, USA*

We developed a robust and low-cost array of virtual Frisch-grid CdZnTe (CZT) detectors coupled to a front-end readout ASIC for spectroscopy and imaging of gamma rays. The array operates as a self-reliant detector module. It is comprised of 36 close-packed 6x6x15 mm^3 detectors grouped into 3x3 sub-arrays of 2x2 detectors with the common cathodes. The front-end analog ASIC accommodates up to 36 anode and 9 cathode inputs. Several detector modules can be integrated into a single- or multi-layer unit operating as a Compton or a coded-aperture camera. We present the results from testing two fully assembled modules and readout electronics. The further enhancement of the arrays' performance and reduction of their cost are possible by using position-sensitive virtual Frisch-grid detectors, which allow for accurate corrections of the response of material non-uniformities caused by crystal defects.

[a)]**Electronic mail**: bolotnik@bnl.gov

I. INTRODUCTION

Large-volume CdZnTe (CZT) gamma-ray detectors can achieve excellent energy-resolution approaching the statistical limits provided that high-quality crystals with a low content of defects are used[1,2]. Unfortunately, such crystals are rare and expensive. To address of the high costs of today's CZT material, we developed arrays of small area, but thick detectors, which can be produced less expensively with high yields. The geometry of such crystals is convenient for using them as the virtual Frisch-grid detectors, which have been under development in our lab for the past several years. A number of improvements that we recently introduced in the design of these detectors[3-5], combined with a newly developed application-specific integrated circuit (ASIC), assured high-performance of the arrays including the ability to veto[6] the response-hindering incomplete charge collection events (ICC) for which significant charge losses occur due to electron trapping by crystal defects. These improvements were combined into our fully operational benchtop unit employing two detector modules and a complete data acquisition system with a user interface. Here, we report on the performance of this instrument used for spectroscopy and imaging of gamma-ray sources.

CZT detectors belong to single type charge carrier devices[1] in which only electrons are collected on the signal electrode while the slow moving holes (or positive ions in the case of gas detectors) are rapidly trapped but still influence amplitudes of the output signals dependently on locations of interaction points. The outmost problem needed to be addressed in any CZT detector design is how to minimize the effect of the trapped carries. At first, a metal electrostatic shielding grid (Frisch-grid) was introduced in early gas ionization chambers[7,8]. The grid, which is transparent enough to allow the electrons to travel to the collecting electrode (anode), physically divides the detector volume in two regions: collecting and signal generating. Another approach is to place the shielding electrode outside the active volume to create a similar shielding effect as if an actual Frisch-grid were placed inside the detector. This approach is particular effective in the case of drift detectors with the large geometrical aspect ratios. As an example, Dmitrenko *et al.*[9] proposed a gas-filled drift ionization chamber (cell) with the drift field shaping strips (virtually-grounded via capacitors) also used for shielding the collecting electrode. A number of detector designs utilizing the virtual Frisch-grid effect have been proposed for CZT detectors with the shielding electrodes placed directly on the side surfaces of the crystals or separated by a thin layer of insulating material: CAPture^{TM}, hemispherical, Frisch-ring, and capacitive Frisch-grid[10-13]. In the latter two cases, the role of the field shaping electrodes is played by the slightly conducting side surfaces of CZT crystals.

Our detectors utilize narrow non-contacting shielding electrodes which could also be used as sensing strips for measuring locations of interaction points. The detectors are mounded side-by-side on the fanout substrate with minimal gaps between

them, and grouped into 2x2 sub-arrays; their cathode contacts are connected together to form a single (common) cathode[3] for each sub-array. Because of the mutual electrostatic shielding of the detector's anodes, we were able to reduce the width of the shielding electrode down to 4-5 mm without compromising the efficiency of shielding, and so place it near the anode. On the other hand, by leaving unshielded the remaining surface of the detectors, we ensure that the common cathode remains sensitive to the positions of the interaction points occurring between the cathode and the location of the virtual Frisch-grid (~4 mm above the anode for this detector's geometry). The common cathode signals provide independent measures of the interaction depths and the electron cloud drift times that we use for electron charge-loss corrections and rejecting the ICC events.

Previously, we fabricated and tested several small array prototypes consisting of 2x2 and 3x3 detectors with common cathodes[3]. We optimized the detector design and assembling procedures. Here, we detail our final design, and discuss the results from testing the performance of the two fully-operational 6x6 detector modules that can be used as building blocks for assembling large-area, high-energy resolution gamma-ray cameras.

II. ARRAY MODULE DESIGN

The array's design utilizes a modular approach with the possibility of easy replacement of individual detectors and producing a large-area detecting plane by plugging side-by-side several different array modules into a single motherboard. Each array consists of the detector board, carrying detectors placed inside the cells of a thin-walled honeycomb holder and the front-end ASIC board. The boards are connected via multi-pin connectors located on the back of the fan-out substrate and the front side of the ASIC board. The backside of the ASIC board has two additional multi-pin connectors that are used for plugging the array modules into the readout motherboard. The current array module is designed to accommodate 36 detectors, divided into 3x3 sub-arrays of 2x2 detectors with common cathodes.

A. Detector holder

The detector holder (Fig. 1) consists of a thin-walled 5-mm-thick plastic honeycomb, attached to the fanout board, and a 0.5-mm-thick plastic grid used for aligning the detectors. The aligning grid and the honeycomb are separated by a 10-mm-thick Teflon frame that insulates the fanout board from the aligning grid and the cathode boards (biased to 2-3 kV). When assembled, the honeycomb and aligning grid form an array of cells for holding the individual detectors in place.

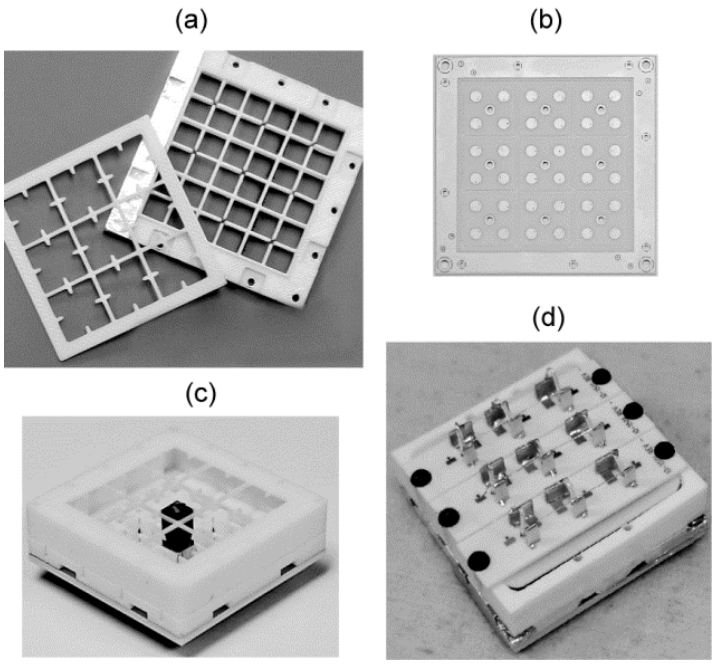

FIG. 1. Components of the detector holder: (a) plastic honeycomb and top alignment grid; (b) fanout substrate; (c) assembled holder attached to the fanout substrate with a detector slid inside the holder's cell; and (d) fully assembled array module.

Each detector from the array is furnished with two CuBe spring contacts mechanically attached the cathode and anode surfaces. The detectors are slid inside the holder cells and gently are pressed to the fanout pads with the cathode boards (Fig. 1). By adjusting the screws on the cathode boards, we can control the load of the spring contacts. The cathode board also connects the cathode of the detectors within each of the 2x2 sub-arrays. The small-footprint decoupling capacitors and high-voltage (HV) bias resistors are attached to the cathode boards. The 4.5-mm-wide CuBe strips, with their miniature spring-finger contacts, are used to ground the shielding electrodes on all the detectors. The strips are inserted inside the slots made in the walls of the plastic honeycomb. The Teflon frame is attached to the fanout board with a set of screws, so providing rigidity to the holder assembly. The backside of the fanout board contains two multi-pin connectors for plugging in the ASIC board.

B. Detectors

Each detector is encapsulated inside an ultra-thin polyester shell[4] enveloping the entire crystal and held in place by two flat CuBe spring contacts on the top (cathode) and bottom (anode) surfaces (Fig. 2). The spring contacts cover the entire area of the cathode- and anode-surfaces. This configuration assures the easy replacement of individual detectors (if necessary), whilst affording good resistance to any shocks or external impacts. As a final step in the fabrication, a 4.5-mm-wide aluminum tape with a thin conducting adhesive layer was wrapped around the detector's sidewalls at the anode side.

Before assembling the arrays, we screened over 100 detectors, acquired from two suppliers, eV Products, Inc. and Redlen, Inc., using white X-ray beam diffraction topography and IR transmission microscopy. After that, we assembled and tested individual detectors and compared their spectral responses with the diffraction topography and IR data. We found strong correlations between the presence of twins and sub-grain boundaries (normally decorated by big Te inclusions) and poor responses of the detectors. The bulk resistivity and the electron $\mu\tau$-product of the material used to fabricate these detectors, as specified by the vendors, respectively were $>3\times10^{10}$ Ohm-cm and $>7\times10^{-3}$ cm^2/V. We selected the best 72 detectors to assemble two 6x6 arrays; for the first array we chose the best 36 detectors. We could not use some detectors because of their excessively high leakage currents that we attributed either to the detectors' leaky side surfaces, or to conductive subgrain boundaries propagating across detectors between the cathode- and anode-contacts. We rejected some because of their poor spectral responses.

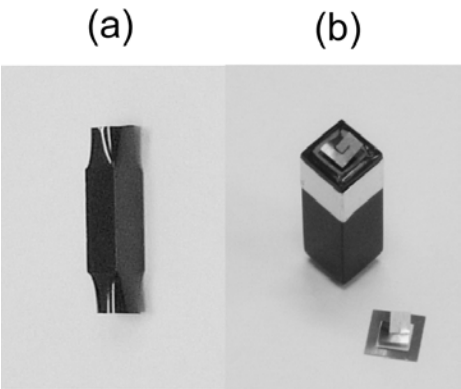

FIG. 2. Assembling virtual Frisch-grid detectors: (a) 6x6x15-mm^3 crystal encapsulated in the ultra-thin polyester shell; (b) encapsulated detector furnished with two spring contacts, and a 5-mm-wide shielding electrode (aluminum tape with a thin conducting adhesive layer).

The virtual Frisch-grid detector operates as a classic ionization chamber with the shielding Frisch-grid[7,8], with well-known response characteristics. Figure 3 shows the dependences of the amplitudes of the cathode and anode signals and their ratio, C/A, versus the drift time measured for a representative detector. We used the dependence of C/A as a merit function for rejecting the ICC events[6].

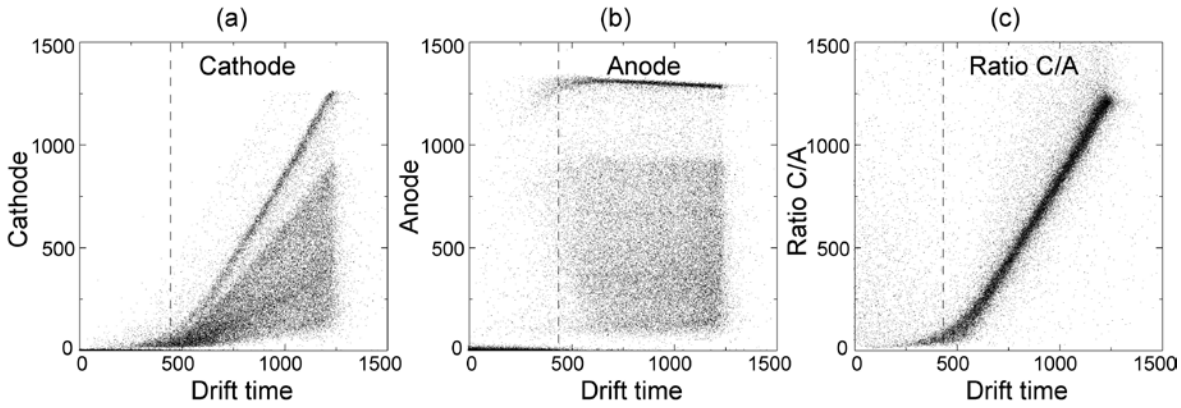

FIG. 3. Dependence of the amplitudes of the cathode (a) and anode (b), and their ratio (c) on the drift time (correlation curves) measured for a 6x6x15 mm^3 virtual Frisch-grid detector with a 5-mm-wide shielding electrode placed near the anode. The signal amplitudes and the drift times are plotted in relative units.

C. AVG ASIC

We developed the low-noise front-end AVG ASIC to accommodate the signals generated on the 36 anodes and 9 cathodes (each detector module is coupled to a single ASIC). The new ASIC mimics the design of its predecessor, the H3D ASIC, developed for 3D position-sensitive pixelated detectors by BNL's Instrumentation Division in collaboration with the University of Michigan[14-16]. A full description of this powerful and multi-functional ASIC was given by De Geronimo *et al.*[14] Here we describe details of its implementation in the new AVG ASIC particularly related to reading out the signals from the array. The AVG ASIC differs by the number of channels, input capacitances (matching to 6x6 mm^2 area anodes), the maximum acceptable leakage currents and the readout logic (it captures and sends out the amplitude and timing information from all the anodes and cathodes for each event).

In general, the charge signals (read out after the charge-sensitive preamplifiers) generated on the anodes and the cathodes contain all information about the ionization event. The beginning of the slow-rising slope of the cathode signals correspond to the moment when the interaction event occurs, while the moment when the fast-rising anode signals reach their maximum level correspond to the times when the electron clouds reach the anodes. The AVG ASIC employs the analog processing of the charge signals. The standard approach employed to extract the amplitude and timing information is to use shaping amplifiers with short- and long-shaping times, which can determine the amount of the charge produced for each interaction event and the electron clouds' drift times. The latter is important for correcting the electron clouds' charge losses and for finding the relative depths of the interaction points. As an example, Fig. 4 shows typical charge signals induced on the

electrodes of the anode and cathode, with the dashed lines marking the time of the interaction event and the arrival time of the electron cloud.

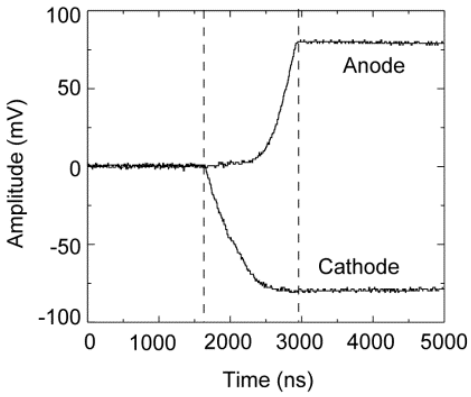

FIG. 4. Typical charge signals generated on the anode and the cathode contacts (unshaped signals from the charge-sensitive amplifiers). The dashed lines mark the time of the interaction event and the arrival time of the electron cloud.

The anode channels implement the conventional processing chain of analog signals. It encompasses a low-noise charge-sensitive amplifier optimized for 3.3-pF input capacitance with a test capacitor and continuous reset adapted to a leakage current up to 50 nA, a baseline stabilizer, a fifth-order unipolar shaping amplifier with an adjustable peaking time, and two peak and timing detectors for measuring the amplitude and timing for both the positive and negative pulses[17-19]. Similarly, the cathode channel implements a charge-sensitive amplifier optimized for a ~ 6.3 pF input capacitance with test capacitor, continuous reset, and leakage currents up to 50 nA; however, it is followed by two parallel filtering- and processing-circuitries, one (with a long shaping time) for measuring the amplitude, and the other (with a short shaping time) for measuring the timing. The anode amplitude-processing circuitry provides a fifth-order unipolar shaping with adjustable peaking times between (0.5-2) μs. The timing assigned to the anode signals is measured at their peaking time (peaking-time method[14]). The main advantage of this method is that, to a first order, it is independent of the signal amplitude. The cathode amplitude-processing circuitry also relies on a fifth-order unipolar shaping with adjustable peaking times between (0.5-2) μs, while the timing-processing section supports four different options for finding the beginning of the cathode signal (see publication by De Geronimo *et al.*[14] for details). One of them, which we used here, is a fifth-order bipolar shaping with adjustable peaking times between (100-800) ns. The internal timing resolution of the ASIC is ~20 ns; however, the actual timing measurements could be strongly affected by the CZT material non-uniformities.

During the acquisition, the ASIC waits for the above-threshold events in any of the 36 anode channels. Once the anode signal exceeds the threshold, the ASIC finds the first peak in the triggered channel, after which it starts capturing the peaks and timings in all 45 channels, even if their signal is below the threshold (i.e., noise). The capture of the peaks proceeds until the acquisition stops. The signal to stop acquisition (common to all channels) is generated in response to the first triggered anode after a delay set by the user. We note that an above-threshold event associated with a negative peak cannot initiate the processing of the peak and timing in other anodes. Normally, the first peak-found signal in each anode is used to generate the timing signal associated with the anode event. However, as an option, the measurement of timing can re-started at the next highest peak rather than at the first peak (this option might be useful for measuring timing on events induced by neighboring detectors before an above-threshold event).

The ASIC converts the timing information into a voltage using a ramp of adjustable length. The ramp starts when the first peak is found, and ceases when the acquisition stops. If the peak is not found within the timeout, although a peak was found in another anode, a local anode reset occurs, and the anode channel will wait for the next peak. If the peak is not found within the timeout, and no peak was found in any other anode, the global acquisition is reset, and the ASIC internally will re-start the entire acquisition cycle. Once the cathode signal exceeds the threshold, the next highest peak will be captured for that channel. The capture of the next highest peak also occurs when any anode event exceeds the threshold. In both cases, the capture of the next highest peak proceeds until the acquisition stops. If the peak is not found within the timeout, a global acquisition reset occurs, and the ASIC internally will restart the entire acquisition cycle.

The ASIC operates at 2.5 V and dissipates ~165 mW of the total power. During the measurements, it demonstrated excellent performance in terms of measuring amplitude and time, with the array biased up to 3000 V, a low trigger threshold of <20 keV, and low electronic noise at (1.5-2.5) keV FWHM, depending on the detector's leakage current.

D. External electronics and data processing

Figure 5 shows the 7x9 mm^2 AVG ASIC chip mounted on the carrier board. Every group of four anode channels is serviced by a common cathode. The ASIC is wire-bonded to the carrier board in a one-to-one mapping scheme to minimize bond length and cross-talk. The carrier board provides additional filtering of the DC supply as close as possible to the ASIC, and each cathode channel is ESD protected with an external diode network. On the front side of the carrier board are two connectors that interface with the mother board. The connector at the top (Fig. 5) provides digital supply, digital ground, and the signals used to communicate with the ASIC. The bottom connector provides an analog interface to the motherboard. The

analog supply, analog ground, the peak amplitude, timing amplitude, and monitor signals are all routed to the analog interface. On the backside of the carrier board, there are two connectors that interface with the detector modules. One connector is reserved for the anode signals and analog ground, while the other is connected to the cathode signals, preamplifier supply, analog supply and analog ground respectively.

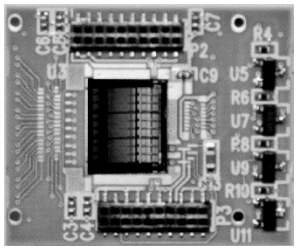

FIG. 5. The AVG ASIC chip mounted on the ASIC board.

For testing the arrays, we fabricated two motherboards, each mechanically supporting up to 4 detector modules via multi-pin connectors. It also carries low-voltage converters supplying power to the ASIC chips, and two ADCs for digitizing the peak amplitudes and timing information from all channels. The motherboard is connected to the communication board containing the FPGA for processing the data and communicating with the ASICs and the USB port. The boards were placed inside the light-tight aluminum test box; since it does not provide cooling to remove the heat generated by the ASIC, we placed the box inside an environmental chamber to maintain the detectors' temperature during the measurements at 17-18 C. Without cooling, the ASIC would generate enough heat to raise the temperature of the CZT detectors inside the closed box to 40 C. During testing, the arrays were irradiated with uncollimated ^{137}Cs, ^{133}Ba, and ^{241}Am sources placed ~2 cm above the cathodes. The cathode's bias was set at 2500 V. We used the full-readout mode of the ASIC, such that any of the detectors from the array could initiate the readout sequence from all channels. For each interaction event, the ASIC sends a stream of data containing the peaks' amplitudes and the corresponding times captured in each of the 45 channels. The data stream was saved in a file in the computer's memory for off-line analysis.

The events could be triggered by any of the 36 detectors as the anode signal exceeds the hardware's threshold, which can be set independently for each of the readout channels. The ratio of the cathode-to-anode signals is used to evaluate the depth of the interaction point with respect to the anode, while the differences between the cathode- and anode- times give the electron clouds' drift times after subtracting the time offsets. (The later also can be used to evaluate the depth of the interaction point.) Both the timing and the interaction depth information can be used to apply the charge-loss correction; however, we found that using of the timing normally gives better performance. There is a small probability of multiple

interactions occurring within a single detector; in such cases, the ASIC reports the averaged amplitude and time as if a single interaction were detected therein.

We use both the amplitudes and times to validate the events; the captured amplitude must rise above the software-selected threshold within a certain time-window set with respect to the trigger. The amplitudes captured from two or more detectors are added to determine the total energy deposited by the incident particles. The positional information also is evaluated for each of the interaction points and can be used for imaging.

For calibrating the detectors' energies, we used the photopeaks generated by standard radioactive sources and the baseline peak. The peak positions and their widths (FWHMs) were evaluated from Gaussian fits. Since the peaks after the drift-time corrections are not represented exactly by a Gaussian function, we also calculated the geometrical widths of the photopeaks at half of their maxima. We note that for Gaussian fitting, we selected the fitting interval defined by two levels relatively to the peak's height: 30% on the left side and 10% on the right.

III. RESULTS FROM THE ARRAYS TESTING

Figures 6-8 show the pulse-height spectra of single interaction point events for all detectors, measured respectively from uncollimated ^{137}Cs, ^{133}Ba, and ^{60}Co sources. The energy resolution for all the detectors lies in a range of 0.7-1.3% FWHM at 662 keV. Correspondingly, the combined spectra are shown in Figs. 9 (a-c). The overall energy resolution was 1.0% at 662 keV for the combined spectra, a very good result taking into account the large cross-section, 6x6 mm^2, of the detectors. The above spectra were corrected using the electron clouds' drift times. We recently demonstrated that with next generation of virtual Frisch-grid detectors, having position-sensing strips, we can further improve the energy resolution by correcting the detector responses in the lateral (X-Y) directions to achieve less than 1% FWHM.

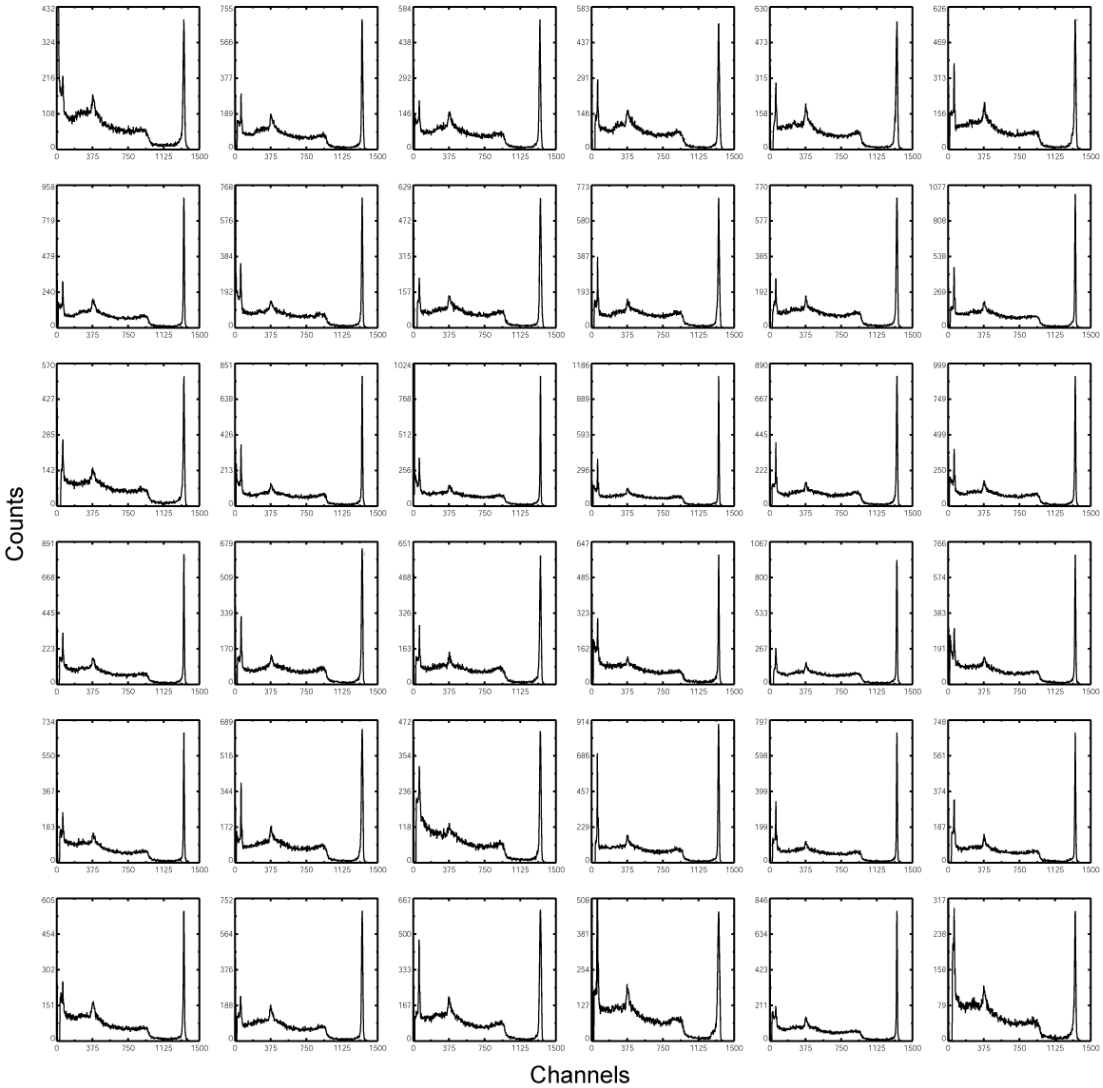

FIG. 6. Pulse-height spectra measured for single-point interaction events from a ^{137}Cs source for all the detectors from the array after the charge-loss corrections.

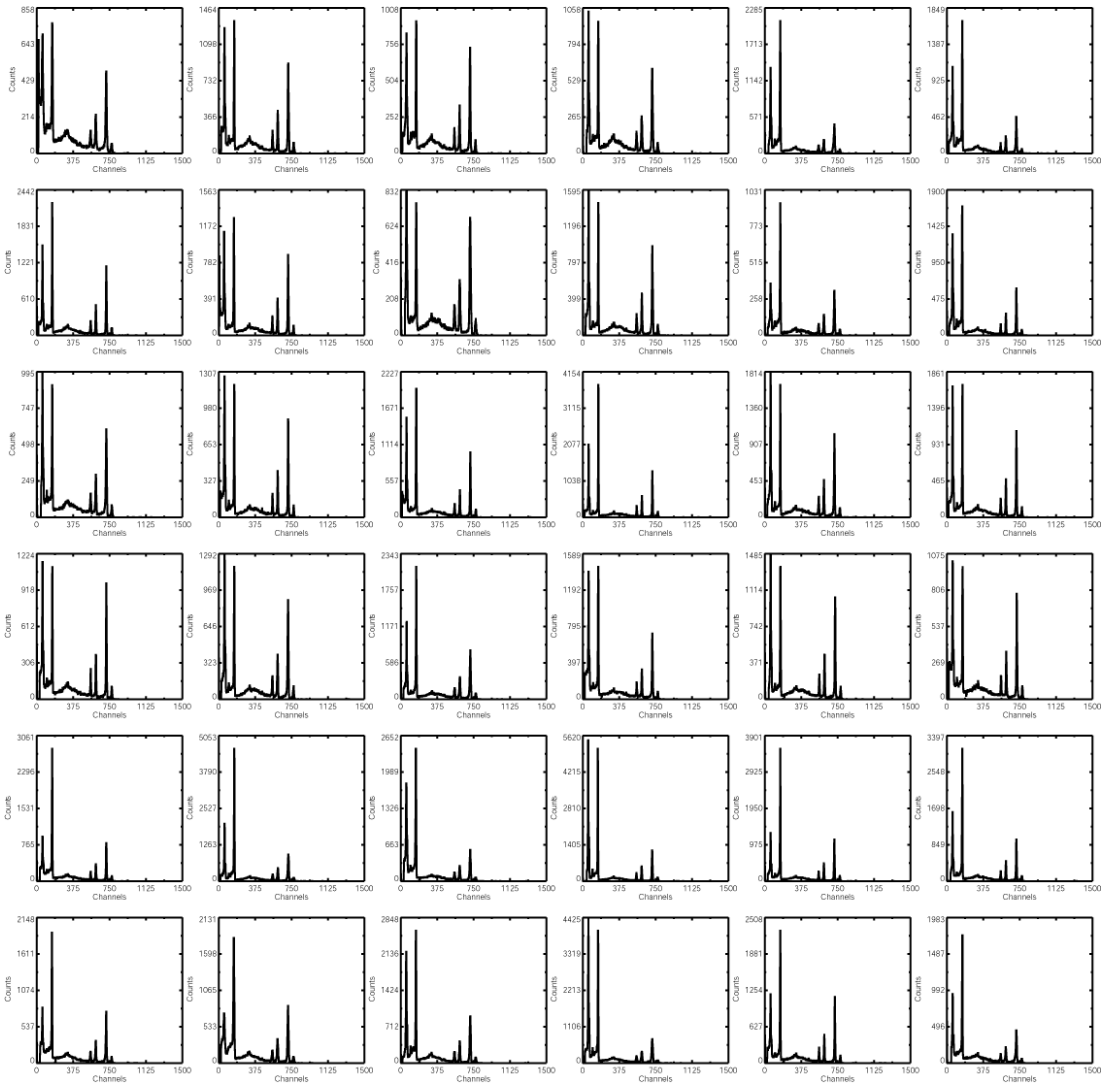

FIG. 7. Pulse-height spectra measured for single-point interaction events from a ^{133}Ba source for all the detectors from the array after the charge-loss corrections.

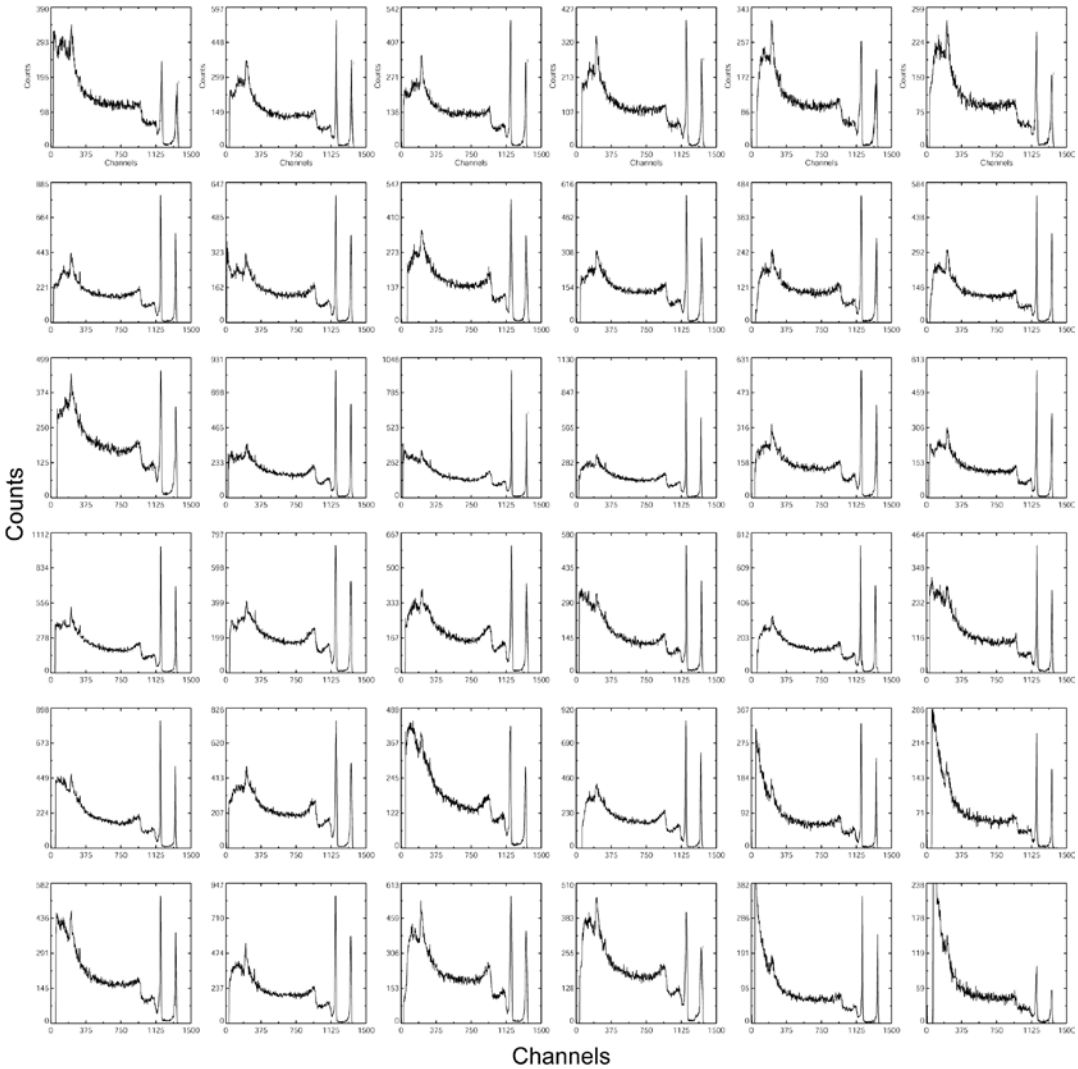

FIG. 8. Pulse-height spectra measured for single-point interaction events from a ^{60}Co source for all the detectors from the array after the charge-loss corrections.

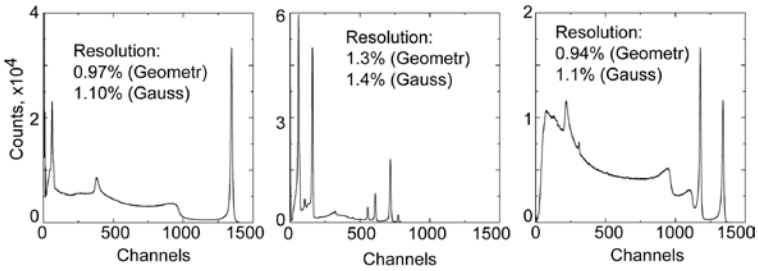

FIG. 9. The combined pulse-height spectra from uncollimated ^{137}Cs, ^{133}Ba, and ^{60}Co sources.

For the second array, we achieved an overall resolution of 1.4% FWHM at 662 keV with a broader range of peak- widths measured for individual detectors. The poorer performance of the second array demonstrates that the energy resolution is determined primarily by the quality of the CZT crystals; when higher-quality crystals are used, the device performance improves significantly. Selecting higher-quality crystals is a straightforward way to improve the performance of the arrays. However, because of the low yield of such crystals, this increases the array cost. Another approach is to extend the acceptance boundaries of CZT crystals by implementing more accurate 3D corrections of the charge loss due to defects. As mentioned before, this can be achieved by employing position-sensitive virtual Frisch-grid detectors that we recently proposed for correcting the non-uniformities in the response caused by the crystal's defects[20]. In this new design, the shielding electrode consists of four separate strips, one on each side. The transient signals induced on these strips are processed to evaluate the positions of the electron clouds in the X-Y plane. Mathematically, it means that with the X- and Y-coordinates, this can be used to correlate the amplitudes of the anode signals to the locations of crystal's defects. This correlation function, which should be measured during calibration of the detector, then is used to correct the anode signals and to improve the detector's spectral response. Fig. 10 illustrates improvements of the energy resolution in four 6x6x15 mm^3 virtual Frisch-grid detectors for two different-quality grades: (a,b) good, and (c,d) poor, after applying the drift-time corrections and after applying corrections along the Z and X-Y directions. As seen, for good detectors, the energy resolutions, which were 1 and 2% FWHM at 662 keV before corrections, were improved to less than 0.7% and 0.8%, respectively. For poor detectors, which have multiple peaks before the corrections and which otherwise would never be used as detectors in a high energy-resolution array, the energy resolutions for the individual detectors improved to below 2%. This approach, which we implement in the next generation of arrays, combined with the rejection of ICC events algorithm allows us to employ less expensive off-the-shelf crystals with higher acceptance yields.

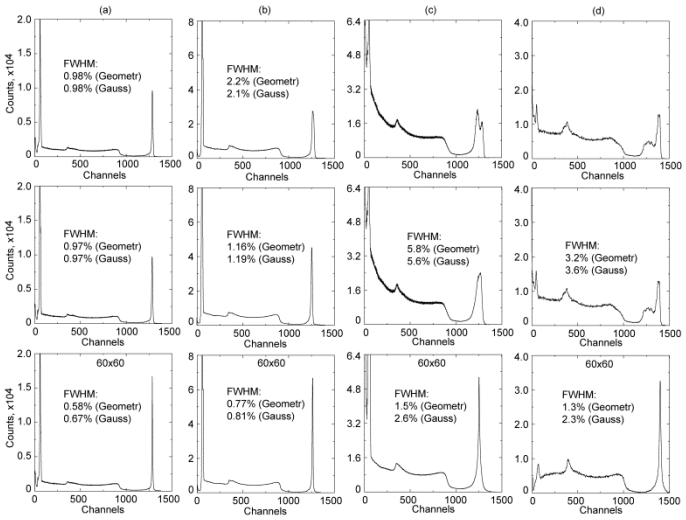

FIG. 10. Pulse-height spectra evaluated for four detectors: (a,b) good material quality, and (c,d) bad material quality. The top row contains the uncorrected spectra without segmentation, and the second row presents the spectra after making the drift-time corrections. The third row shows the spectra evaluated after electronically segmenting the anodes into 60x60 pixels, and applying the drift-time corrections for each voxel before equalizing the peak positions.

Finally, we demonstrate the feasibility of using the arrays as Compton cameras. Here, we describe the simplest case of using a single array. Applying the Compton reconstruction technique, we can identify a direction to the source. As illustrated in Fig. 11 (left), when radiation is scattered in one detector and absorbed in one of the others, the scattering angle can be calculated from the energy deposited at each interacted detector. With the scattering angle and positions of interaction points, a back-projection cone containing the actual direction to the source can be drawn (green line). After measuring many events, we can estimate the direction to the source based on the superposition of back projections (Fig. 11 (right)).

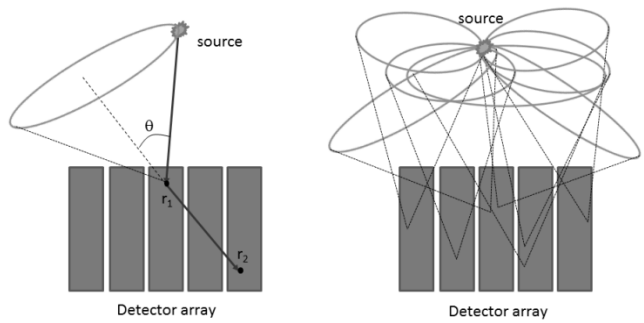

FIG. 11. Compton reconstruction: (a) Back projection of a Compton cone; and, (b) identified direction to the source based on the superposition of multiple cones.

We implemented this algorithm in practice by using measurements with an uncollimated ^{137}Cs source placed at ~45 degree off the normal axes at ~30 cm from the detector's center. We applied the Maximum Likelihood Expectation Maximization Algorithm[21] (30 iterations) to reconstruct the direction to the source. Figure 12 shows the "image" of the source in the altitude azimuth coordinate system, which demonstrates that the array can give the direction to the location of the radioactive source. Because the X-Y position resolution is limited by the crystal size, the device shows a very modest angular resolution, which can be improved greatly by using the new position-sensitive virtual Frisch-grid detectors. The details of these measurements with position-sensitive virtual Frisch-grid detectors will be published separately[22].

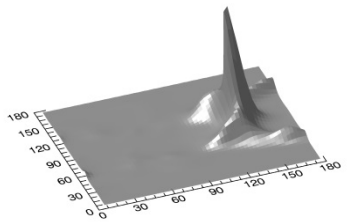

FIG.12. Image of an uncollimated ^{137}Cs source located at ~30 cm away from, and ~45 degree off the normal axes. In the plot, the range of the axes is 180 degrees.

IV. CONCLUSIONS

We demonstrated performance of a robust self-reliant detector module, consisting of an array of virtual Frisch-grid CZT detectors and front-end readout ASIC, proposed for assembling into large-area high-energy resolution, position-sensitive gamma cameras. The array is comprised of 36 close-packed 6x6x15 mm^3 detectors grouped into 3x3 sub-arrays of 2x2 detectors with common cathodes.

We assembled and tested two modules. For the first array, assembled from the better CZT detectors, we achieved an energy resolution of <1.0% FWHM at 662 keV. For the second array, assembled from the more typical quality detectors, we obtained 1.4% FWHM. We also demonstrated the feasibility of using the arrays as Compton cameras to identify the direction of the gamma-ray source.

Use of position-sensitive virtual Frisch-grid detectors will further improve the response of the CZT detectors for crystals with a high content of defects and, thus, increase the acceptance rate of the CZT crystals and performance of the fabricated detectors, so lowering their cost and improving their spectroscopic and imaging capabilities.

ACKNOWLEDGMENTS

This work was supported by U.S. Department of Energy, Office of Nonproliferation and Verification Research & Development, DNN R&D, U.S. Defense Threat Reduction Agency (DTRA) and BNL's Technology Maturation Award. The manuscript has been authored by Brookhaven Science Associates, LLC under Contract No. DE-AC02-98CH1-886 with the U.S.

REFERENCES

[1]G. Knoll, Radiation Detection and Measurement, 4th ed., Wiley, 2010.

[2]Z. He, W. Li, G. E Knoll, D. K. Wehe, J. Berry, C. M. Stahle, “3-D position sensitive CdZnTe gamma-ray spectrometers”, Nucl. Instr and Meth., A422, 173-178 (1999).

[3]A. E. Bolotnikov, J. Butcher, G. S. Camarda, Y. Cui, G. De Geronimo, J. Fried, P. M. Fochuk, A. Hossain, KiHyun H. Kim, O. V. Kopach, G. Mahler, M. Marshall, B. McCall, M. Petryk, E. Vernon, G. Yang, and R. B. James, “Design Considerations and Testing of Virtual Frisch-Grid CdZnTe Detector Arrays Using the H3D ASIC”, IEEE Trans. Nucl. Sci., 60 (4), 2875-2882 (2013).

[4]A. E. Bolotnikov, G. S. Camarda, Y. Cui, G. De Geronimo, J. Fried, R. Gul, A. Hossain, K. H. Kim, E. Vernon, G. Yang, and R. B. James, “Array of Virtual Frisch-Grid CZT Detectors with Common Cathode Readout for Correcting Charge Signals and Rejecting Incomplete Charge-Collection Events”, IEEE Trans. Nucl. Sci., 59 (4), 1544-1551 (2012).

[5]J. K. Polack, M. Hirt, J. Sturgess, N. D. Sferrazza, A. E. Bolotnikov, S. Babalola, G. S. Camarda, Y. Cui, S. U. Egarievwe, P. M. Fochuk, R. Gul, A. Hossain, K. Kim, O. V. Kopach, L. Marchini, G. Yang, L. Xu, R. B. James, “Variation of electric shielding on virtual Frisch-grid detectors”, Nucl. Instr. and Meth., A621, 424-430 (2010).

[6]A. E. Bolotnikov, G. S. Camarda, Y. Cui, G. De Geronimo, J. Fried, R. Gul, A. Hossain, K. Kim, G. Yang, E. Vernon, and R. B. James, “Rejecting incomplete charge-collection events in CdZnTe and other semiconductor detectors,” Nucl. Instr. Meth., A664, 317–323 (2012).

[7]O. R. Frisch, Unpublished report, BR-49, “Isotope analysis of uranium samples by means of their alpha-ray groups”, British Atomic Energy Project (1944).

[8]O. Buneman, T. E. Cranshaw, and J. A. Harvey, “Design of Grid Ionization Chambers,” Can. J. Res., A27, 191-206 (1949).

[9]V.V. Dmitrenko, A.C. Romanuk, Z.M. Uteshev, V.K. Chernyatin, “Spectrometric applications of an ionization-type drift chamber”, Pribory I Tekhnika Eksperimenta v.1, pp. 51-53, 1982. Translation in Instruments and Experimental Techniques (USA), vol. 25, n. 1, pp. 50-53 (1982).

[10]K. Parnham, C. Szeles, K. G. Lynn, and R. Tjossem, "Performance Improvement of CdZnTe Detectors Using Modified Two-Terminal Electrode Geometry," Hard X-ray, Gamma-Ray and Neutron Detector Physics, Proceedings of SPIE, Vol. 3786, pp. 49-54, 1999.

[11]C. Szeles, D. Bale, J. Grosholz, Jr., G. L. Smith, M. Blostein, and J. Eger, "Fabrication of High Performance CdZnTe Quasi-Hemispherical Gamma-ray CAPture™ Plus Detectors", Hard X-Ray and Gamma-Ray Detector Physics VIII, edited by Larry A. Franks, Arnold Burger, and Ralph B. James, Proceedings of SPIE Vol. 6319 (SPIE, Bellingham, WA, 2006).

[12]D. S. McGregor and R. A. Rojeski, U.S. patent 6175120 (January 16, 2001).

[13]G. Montemont, M. Arques, L. Verger, and J. Rustique, "A capacitive Frisch grid structure for CdZnTe detectors," IEEE Trans. Nucl. Sci., 48 (3) 278-281 (2001).

[14]G. De Geronimo, E. Vernon, K. Ackley, A. Dragone, J. Fried, P. O'Connor, Z. He, C. Herman and F. Zhang, "Readout ASIC for 3D Position-Sensitive Detectors", IEEE Trans. Nucl. Sci., 55 (3), 1593-1603 (2008).

[15]E. Vernon, K. Ackley, G. De Geronimo, J. Fried, P. O'Connor, Z. He, C. Herman, and F. Zhang, "ASIC for high rate 3-D position sensitive detectors," IEEE Trans. Nucl. Sci., 57 (3), 1536-1542 (2010).

[16]F. Zhang, C. Herman, Z. He, G. De Geronimo, E. Vernon, and J. Fried, "Characterization of the H3D ASIC readout system and 6.0 cm^3 3-D position sensitive CdZnTe Detectors," IEEE Trans. Nucl. Sci., 59, 236-242 (2012).

[17]G. De Geronimo and P. O'Connor, "MOSFET optimization in deep submicron technology for charge amplifiers", IEEE Trans. Nucl. Sci., 52 (6), 3223-3232 (2005).

[18]G. De Geronimo and P. O'Connor, "A CMOS fully compensated continuous reset system", IEEE Trans. Nucl. Sci., 47 (4), 1458-1462 (2000).

[19]G. De Geronimo, P. O'Connor, and J. Grosholz, "A CMOS baseline holder (BLH) for readout ASICs", IEEE Trans. Nucl. Sci., 47 (3), 818-822 (2000).

[20]A. E. Bolotnikov, G. S. Camarda, Y. Cui, G. De Geronimo, J. Fried, A. Hossain, K. Lee, G. Mahler, M. Maritato, M. Marshall, M. Petryk, U. Roy, E. Vernon, G. Yang and R. B. James, "Use of high-granularity position sensing to correct response non-uniformities of CdZnTe detectors", Appl. Phys. Lett., 104, 263503 (2014).

[21]L. Parra and H. H. Barrett, "List-mode likelihood: EM algorithm and image quality estimation demonstrated on 2-D PET," IEEE Trans. Med. Imag., 17 (2), 228–235 (1998).

[22]W. Lee, A.E. Bolotnikov, T. Lee, G.S. Camarda, Y. Cui, R. Gul, A. Hossain, U. Roy, G Yang, and R.B. James, "Mini Compton Camera Based on an Array of Frisch-grid CdZnTe Detectors", submitted to IEEE Trans. Nucl. Sci. (2015).

LIST OF FIGURES

FIG. 1. Components of the detector holder: (a) plastic honeycomb and top alignment grid; (b) fanout substrate; (c) assembled holder attached to the fanout substrate with a detector slid inside the holder's cell; and (d) fully assembled array module.

FIG. 2. Assembling virtual Frisch-grid detectors: (a) 6x6x15 mm^3 crystal encapsulated in the ultra-thin polyester shell; (b) encapsulated detector furnished with two spring contacts, and a 5-mm-wide shielding electrode (aluminum tape with a thin conducting adhesive layer) [2].

FIG. 3. Dependence of the amplitudes of the cathode (a) and anode (b), and their ratio (c) on the drift time (correlation curves) measured for a 6x6x15 mm^3 virtual Frisch-grid detector with a 5-mm-wide shielding electrode placed near the anode. The signal amplitudes and the drift times are plotted in relative units.

FIG. 4. Typical charge signals generated on the anode and the cathode contacts (unshaped signals from the charge-sensitive amplifiers).

FIG. 5. The AVG ASIC chip mounted on the ASIC board.

FIG. 6. Pulse-height spectra measured for single-point interaction events from a ^{137}Cs source for all the detectors from the array after the charge-loss corrections.

FIG. 7. Pulse-height spectra measured for single-point interaction events from a ^{133}Ba source for all the detectors from the array after the charge-loss corrections.

FIG. 8. Pulse-height spectra measured for single-point interaction events from a ^{60}Co source for all the detectors from the array after the charge-loss corrections.

FIG. 9. The combined pulse-height spectra from uncollimated ^{137}Cs, ^{133}Ba, and ^{60}Co sources.

FIG. 10. Pulse-height spectra evaluated for four detectors: (a,b) good material quality, and (c,d) bad material quality. The top row contains the uncorrected spectra without segmentation, and the second row presents the spectra after making the drift-

time corrections. The third row shows the spectra evaluated after electronically segmenting the anodes into 60x60 pixels, and applying the drift-time corrections for each voxel before equalizing the peak positions.

FIG. 11. Compton reconstruction: (a) Back projection of a Compton cone; and, (b) identified direction to the source based on the superposition of multiple cones.

FIG.12. Image of the uncollimated ^{137}Cs source located at ~30 cm away from, and ~45 degree off the normal axes. In the plot, the range of the axes is 180 degrees.